Macro-elasticity of granular materials composed of polyhedral particles

Duc Chung Vu, Lhassan Amarsid, Jean-Yves Delenne, Vincent Richefeu, Farhang Radjai

Macro-elasticity of granular materials composed of polyhedral particles

Duc Chung Vu[1,2], Lhassan Amarsid[1], Jean-Yves Delenne[3], Vincent Richefeu[4], Farhang Radjai[2*]

[1]CEA, DES, IRESNE, DEC, SESC, LDOP, Saint Paul les Durance, 13108, France.
[2*]LMGC, CNRS, University of Montpellier, Montpellier, 34090, France.
[3]IATE, INRAE, Institut Agro, University of Montpellier, Montpellier, 34000, France.
[4]3SR, CNRS, University of Grenoble Alpes, Grenoble, 38400, France.

*Corresponding author(s). E-mail(s): franck.radjai@umontpellier.fr;
Contributing authors: duc-chung.vu@umontpellier.fr; lhassan.amarsid@cea.fr;
jean-yves.delenne@umontpellier.fr; vincent.richefeu@3sr-grenoble.fr;

Abstract

Particle shape variability is a key to understanding the rich behavior of granular materials. Polyhedra are among the most common particle shapes due to their ubiquitous origins in nature such as rock fragmentation and mineral crystallisation. Because of their faceted shape, polyhedral particles tend to assemble in jammed structures in which face-face and face-edge contacts between particles control the packing-level properties. In this paper, we use tri-periodic particle dynamics simulations to derive for the first time a generic analytical expression of the elastic moduli of polyhedral and spherical particle packings subjected to triaxial compression as a function of two contact network variables: 1) a "constraint number" that accounts for the face-face and edge-face contacts between polyhedra and is reduced to the coordination number in the case of spherical particles, and 2) the contact orientation anisotropy induced by compression. This expression accurately predicts the simulated evolution of elastic moduli during compression, revealing thereby the origins of the higher elastic moduli of polyhedral particle packings. We show that particle shape affects the elastic moduli through its impact on the contact network and the level of nonaffine particle displacements is the same for the simulated shapes. Its nearly constant value during compression underlies the constant values of our model parameters. By connecting the elastic moduli to the contact network through parameters that depend on particle shape, our model makes it possible to extract both the connectivity and anisotropy of granular materials from the knowledge of particle shape and measurements of elastic moduli.

Keywords: Granular materials, Particle dynamics method, Polyhedral particles, Elastic moduli, Effective Medium Theory, Triaxial compression, Connectivity, Contact orientation anisotropy

1 Introduction

Granular materials have been at the focus of extensive research for their rich and complex properties rooted in dissipative particle interactions, disordered microstructure, and particle characteristics such as shape and size distribution [1–3]. Although hard-sphere packing has often been used

as a model of granular materials, aspherical particle shape is omnipresent in nature and industry. The crucial role of realistic particle shape for quantitative prediction of the strength and space-filling properties of granular materials has been clearly evidenced by recent simulations and experiments [4–18]. For example, packings composed of particles slightly deviating from spherical shape are more compact than sphere packings whereas larger deviations towards more elongated or platy shapes lead to significantly lower packing fraction [4, 7, 9].

Among diverse particle shapes, regular and irregular polyhedral particles are quite common due to their ubiquitous origins such as rock fragmentation and mineral crystallisation. Their specific feature is to assemble in structures involving face-face and edge-face contacts which, in contrast to simple contact points between spheres, provide a finite support for the contact force. Particle dynamics simulations have shown that such contacts in packings of polyhedral particles are less in number but they capture strong force chains and carry thereby a much higher average force than simple contacts [6, 10]. The microstructure has also been analyzed as a function of the number of facets in relation to shear strength [10, 11, 15]. However, we are aware of no published work on the elastic properties of polyhedral particle packings.

Past work on granular elasticity has essentially focussed on isotropic sphere packings [19–22]. The bulk and shear moduli are proportional to k_n/d, where k_n is the normal contact stiffness and d is mean particle diameter. The moduli depend also on the number of contacts per unit volume, and stiffness ratio k_t/k_n, where k_t is the tangential contact stiffness [21–25]. It is well known that, because of its failure to account for the non-affine nature of particle displacements in granular media, the effective medium theory (EMT) overestimates the elastic moduli [26, 27]. The origins of elastic moduli in the general case of anisotropic sheared media and the effects of particle shape mediated by microstructure and nonaffine displacements are therefore widely open issues.

We report in this paper on a detailed investigation of the elastic moduli of dodecahedral (12 faces), icosahedral (20 faces), and spherical particle packings by means of extensive particle dynamics simulations based on the discrete element method (DEM) with a proper treatment of the contact interactions between polyhedral particles. In particular, each face-face interaction is reduced to a set of elastic/frictional contacts between the edges composing the two faces. This allows the geometrical constraints associated with rigid faces to be imposed and the overlaps between the edges are used to compute point forces according to a linear dashpot-spring force law.

Initially isotropic random close packings were prepared by isotropic compaction at zero friction, representing the unique reproducible densest state of each shape. Subjecting then each packing to quasi-static triaxial compression with tri-periodic boundary conditions and a non-zero friction coefficient between particles, we calculated their five orthotropic elastic moduli at regular strain intervals together with contact network variables such as connectivity and contact anisotropy. A key finding is that the elastic moduli can be fully expressed as a function of connectivity and anisotropy with a functional form that does not depend on particle shape, but involve coefficients that depend on particle shape. Accurate determination of these coefficients makes it therefore possible to nicely predict the evolution of elastic moduli with strain. These expressions also reveal how the face-face and face-edge contacts enhance the elastic moduli compared to sphere packings.

In the following, we first introduce numerical procedures. Then, we discuss in Section 3 the evolution of sample-level variables during triaxial compression. The evolution of elastic moduli will be presented in Section 4. In Section 5, we consider the evolution of microstructural variables. In Section 6, we introduce our expression of elastic moduli as a function of microstructural variables by a detailed comparison between the predictions of EMT and our numerical data. Finally, we discuss the most salient results of this paper.

2 Numerical procedures

The simulations were carried out by means of an in-house code based on DEM [28–30]. The interactions between polyhedral particles need a model for face-face and face-edge contacts. The vertex-face and edge-edge interactions involve a single contact point, which can be treated in the same way as the contacts between spherical or smooth convex particles. Such simple contacts represent a

single unilateral constraint, which is treated either by a penalty approach, i.e. introducing a repulsive force depending on the overlap, or by means of Lagrange multipliers as in the Contact Dynamics method [31–33]. In contrast, in the case of a face-face interaction, there are three steric constraints that must be correctly treated to avoid interpenetration between the two particles as a result of their relative normal displacement or rotations around the two other axes.

For rigid polyhedral particles with their finite faces defined by their contours composed of several edges, a face-face interaction can be reduced to interactions between edges composing the two faces or between a vertex and one of the faces [28]. This means that a face-face interaction is reduced to a set of contact points, as shown in Fig. 1(a). If a penalty approach is applied to all contact points, the three constraints will be fully satisfied. It is noteworthy that, the number of contact points can be large depending on the number of edges, but the number of independent constraints is always 3 due to the rigidity of the particles. Similar considerations apply as well to edge-face interactions, which involve two independent steric constraints; see Fig. 1(b). We may thus refer to the face-face and face-edge interactions as *triple* and *double* contacts, respectively.

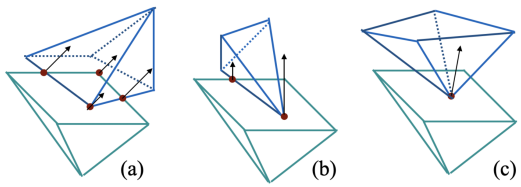

Fig. 1 Different types of contacts between two polyhedra: (a) face to face, (b) face to edge, (c) vertex to face.

The contact points between polyhedral particles are detected by considering separately the sub-elements (vertices, edges and faces). At each contact point, either a linear or a nonlinear force law is implemented. As for Hertz contacts, the nonlinear interactions arise from the curvature of the surface at the contact points (e.g. between two edges modeled as cylinders). However, in this paper we are interested in the effects of particle shape and contact network anisotropy, and therefore we used linear contact laws to reduce computational cost. The normal force law is defined as follows [2, 33–35]:

$$f_n = \begin{cases} 0, & \tilde{f}_n \leq 0, \\ \tilde{f}_n, & \tilde{f}_n > 0, \end{cases} \tag{1}$$

where $\tilde{f}_n = -k_n\delta_n - \gamma\dot{\delta}_n$, k_n is normal stiffness, δ_n is overlap (with sign convention that $\delta_n < 0$ when two particle overlap), $\dot{\delta}_n$ is the relative normal velocity, and γ is the viscous damping coefficient. The tangential force is governed by the Coulomb friction law given by

$$f_t = -min\{k_t\delta_t,\ \mu_s f_n\}sgn(\dot{\delta}_t), \tag{2}$$

where k_t is tangential stiffness, δ_t is cumulative tangential displacement, $\dot{\delta}_t$ is relative tangential velocity, and μ_s is the interparticle friction coefficient.

3 Triaxial compression

We prepared three samples composed of monodisperse particles of dodecahedral, icosahedral, and spherical shapes enclosed in a 3-periodic cubic cell [36–38]. They had exactly the same number of particles (8000), values of parameters, and boundary conditions. We first applied an isotropic compression with zero friction between particles, leading to dense isotropic states corresponding to a random closed packing (RCP) of solid fraction $\Phi \simeq 0.648$ for dodecahedral particles, $\Phi \simeq 0.632$ for icosahedral particles, and $\Phi \simeq 0.637$ for spherical particles.

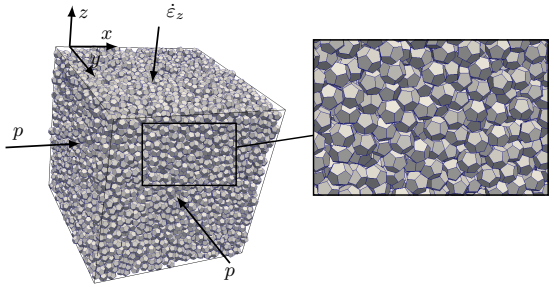

Fig. 2 A snapshot of the sample of dodecahedral particles in the isotropic state.

The isotropic samples were sheared by triaxial compression for four values of friction coefficient $\mu_s = 0.1$, 0.2, 0.3, and 0.4 between particles. The compression was applied along the z axis by imposing a constant strain rate $\dot{\varepsilon}_z$ while keeping the same stress p in lateral directions x and y. The simulation box can expand along these directions to accommodate the applied compression. Since the material is in an initially dense state, the packing dilates and the packing fraction declines towards a stead-state value in all simulations. The inertial number $I = \dot{\varepsilon}_z d(\rho/p)^{1/2}$, where ρ is the particle density and d is the mean particle diameter, is low enough ($< 10^{-3}$) to qualify the compression as quasi-static [33, 39, 40]. By symmetry, the principal stresses and strain rates coincide with the three space directions with σ_1 and ε_1 along the z direction, $\sigma_2 = \sigma_3 = p$, and $\varepsilon_2 \simeq \varepsilon_3$.

Figure 3 shows the evolution of stress ratio q/p, where $q = (\sigma_1 - \sigma_2)/3$ is stress deviator and $p = (\sigma_1 + \sigma_2 + \sigma_3)/3$ is mean stress, as well as the packing fraction Φ as a function of shear strain $\varepsilon_q = \varepsilon_z - \varepsilon_x$ for dodecahedral and spherical particle packings (the trends being similar for icosahedral particles). Due to the initially high value of packing fraction, the samples yield only when q/p reaches a threshold where plastic deformation can begin as a result of particle rearrangements and dilation. Beyond this point, q/p continues to increase to a peak value before slowly decreasing towards a residual plateau at $\sim 60\%$ of shear strain. The peak value reflects therefore the initially high packing fraction although no shear bands develop in our system due to three-periodic boundary conditions. The peak value increases with μ_s. In polyhedra packings the peak stress ratio is higher and the effect of friction coefficient is more pronounced as compared to sphere packings. Since the initial packing fraction is high, Φ decreases gradually before reaching a nearly constant value. The reduction of Φ increases when μ_s is larger. This effect is more pronounced in the case of polyhedral particle packing.

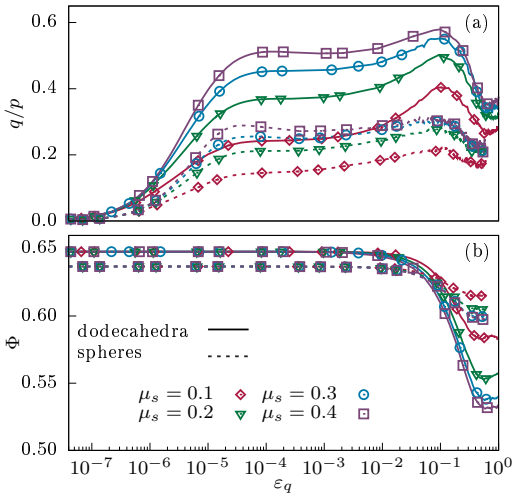

Fig. 3 Stress ratio q/p (a), and packing fraction Φ (b) versus shear strain ε_q for packings of spherical and dodecahedral particles with four values of friction coefficient μ_s. The dashed and solid lines join data points for spheres and dodecahedra, respectively. The symbols represent instances where strain probes are applied.

4 Evolution of elastic moduli

Due to axial symmetry, there are 5 independent moduli C_{ij}, defined as follows, based on the Voigt notation [41, 42]:

$$\begin{bmatrix} \delta\sigma_{11} \\ \delta\sigma_{22} \\ \delta\sigma_{33} \\ \delta\sigma_{23} \\ \delta\sigma_{31} \\ \delta\sigma_{12} \end{bmatrix} = \begin{bmatrix} C_{11} & C_{12} & C_{12} & 0 & 0 & 0 \\ C_{12} & C_{22} & C_{23} & 0 & 0 & 0 \\ C_{12} & C_{23} & C_{22} & 0 & 0 & 0 \\ 0 & 0 & 0 & 2C_{44} & 0 & 0 \\ 0 & 0 & 0 & 0 & 2C_{55} & 0 \\ 0 & 0 & 0 & 0 & 0 & 2C_{55} \end{bmatrix} \begin{bmatrix} \delta\varepsilon_{11} \\ \delta\varepsilon_{22} \\ \delta\varepsilon_{33} \\ \delta\varepsilon_{23} \\ \delta\varepsilon_{31} \\ \delta\varepsilon_{12} \end{bmatrix} \quad (3)$$

The elements C_{11} and C_{22} are the longitudinal moduli, C_{44} and C_{55} are the shear moduli, and C_{12} and C_{23} are the off-diagonal moduli. The bulk modulus K is given by $K = (C_{11} + 4C_{12} + 2C_{22} + 2C_{23})/9$. To determine the moduli, we applied two distinct strain probes in two different directions.

To compute the elastic moduli, we used the sheared samples at 16 instances of their evolution and applied a small strain increment $\delta\varepsilon_{ij}$ to obtain the corresponding stress response $\delta\sigma_{ij}$, from which the elastic moduli were extracted. The sample was allowed to relax to a fully static state before the application of the strain probe. The response is elastic if there are no particle rearrangements, and, as we shall see below, this is the case when $\delta\varepsilon_{ij} < 10^{-5}$.

To determine all elastic moduli, two distinct strain probes in two different directions were

applied at a given stage of evolution of the system. For the first probe, a small strain rate $\dot{\varepsilon}$ was imposed along the z direction while a constant pressure was applied along the directions x and y. Due to axial symmetry, we have $\varepsilon_{22} \simeq \varepsilon_{33}$ and $\delta\sigma_{22} = \delta\sigma_{33} = 0$. Hence, from the general stress-strain relation, we have

$$\begin{cases} C_{11}\varepsilon_{11} + 2C_{12}\varepsilon_{22} = \delta\sigma_{11}, \\ 2C_{55}\varepsilon_{12} = \delta\sigma_{12}, \\ C_{12}\varepsilon_{11} + (C_{22} + C_{23})\varepsilon_{22} = 0. \end{cases} \quad (4)$$

For the second probe, $\dot{\varepsilon}$ was imposed along the y direction while keeping a constant pressure along z and x directions. Therefore, we have $\delta\sigma'_{11} = \delta\sigma'_{33} = 0$ and the stress-strain relations are

$$\begin{cases} C_{12}\varepsilon'_{11} + C_{22}\varepsilon'_{22} + C_{23}\varepsilon'_{33} = \delta\sigma'_{22}, \\ 2C_{44}\varepsilon'_{23} = \delta\sigma'_{23}, \\ C_{11}\varepsilon'_{11} + C_{12}\varepsilon'_{22} + C_{12}\varepsilon'_{33} = 0, \\ C_{12}\varepsilon'_{11} + C_{23}\varepsilon'_{22} + C_{22}\varepsilon'_{33} = 0. \end{cases} \quad (5)$$

From the applied stress and strain increments, we use Eqs. (4) and (5) to calculate all elastic moduli. Note that there are only 5 independent moduli while we have 7 equations. The consistency of the values obtained in this way for the six moduli was verified by checking the following relation imposed by axial symmetry:

$$C_{22} - C_{23} = 2C_{44}. \quad (6)$$

In all cases, we find that this relation holds within an error of 1% in the initially fully elastic regime and up to 10% around the stress peak, where the response to the applied strain probe may involve a plastic component due to softening and unstable particle rearrangements.

It is noteworthy that, since the simulations are based on linear contact laws with constant stiffness parameters k_n and k_t, our packings have an inherent stress scale $E^* = k_n/d$ with which all moduli are expected to scale. In the rigid-particle limit, the condition $p/E^* \ll 1$ should be satisfied. In our simulations, we have $p/E^* \simeq 4.10^{-6}$. The normalized elastic moduli depend also on the stiffness ratio $\alpha_t = k_t/k_n$ [19, 21, 43]. In this work, we set $\alpha_t = 0.8$ in all simulations.

Figures 4, 5, and 6 display the evolution of the longitudinal moduli C_{11} and C_{22}, off-diagonal moduli C_{12} and C_{23}, the shear moduli C_{44} and C_{55}, and the bulk modulus K for packings of spherical and dodecahedral particles together with theoretical predictions that will be discussed in Section 6. The moduli of the polyhedral particle packings at each instance of shear are generally above those of spherical particle packings. They are constant and independent of μ_s at very small shear strains ($< 10^{-5}$), but they change significantly at larger strains when slip events at persistent contacts increase in number and intensity; see Fig. 7.

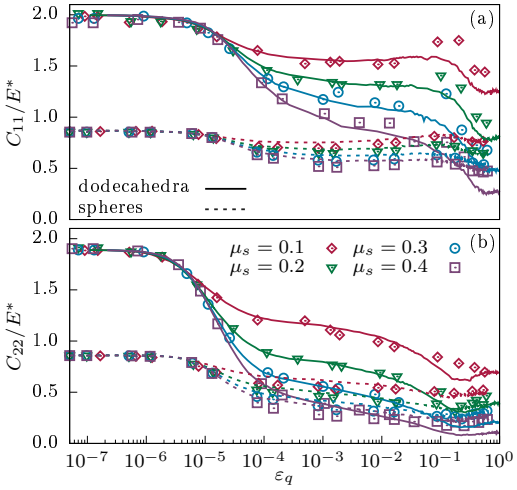

Fig. 4 Normalized longitudinal elastic moduli (a) C_{11}/E^* and (b) C_{22}/E^*, as a function of shear strain ε_q for packings of spherical and dodecahedral particles with different values of friction coefficient μ_s. The dashed and solid lines are theoretical predictions (Eq. (29)) for packings of spheres and dodecahedra, respectively.

The behavior beyond this elastic limit is rather complex. All moduli first decline to values all the more small that the friction coefficient is large. Then, they increase again or continue to decrease slightly depending on particle shape and μ_s, followed by a slight increase or decrease for $\varepsilon_q > 0.1$. Note that the ratio C_{11}/C_{22} increases to values as large as 4 before decreasing to ~ 2, a value previously reported for dense granular materials with low coordination number [23, 44].

5 Evolution of microstructure

The evolution of elastic moduli reflects that of the granular microstructure encoded in the force-bearing contact network. The lowest-order

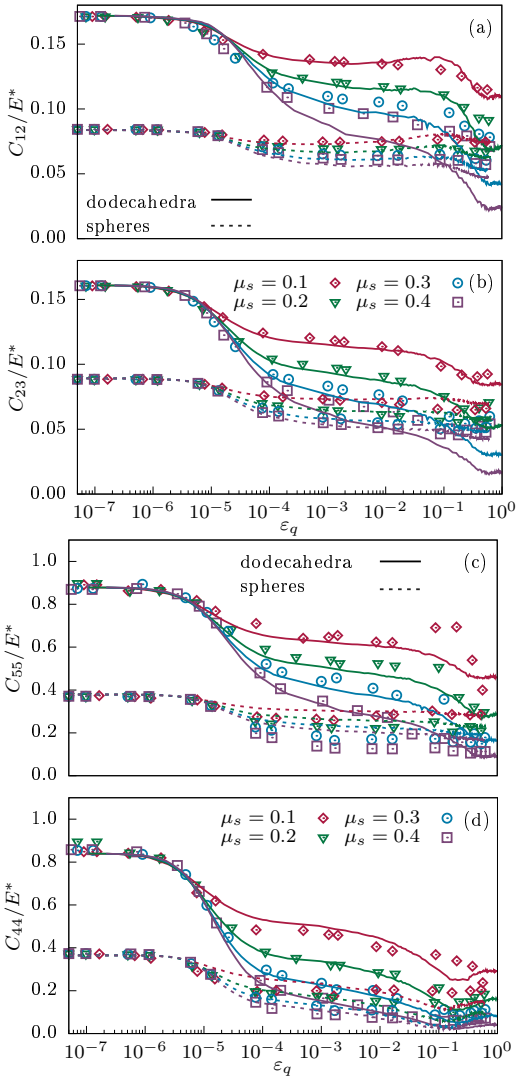

Fig. 5 Normalized elastic moduli: off-diagonal moduli, (a) and (b), and shear moduli, (c) and (d), as a function of shear strain ε_q for packings of spherical and dodecahedral particles with different values of friction coefficient μ_s. The lines are predictions by our proposed expression (29).

descriptors of granular microstructure are the coordination number Z and contact orientation anisotropy a_c [45, 46]. The latter can be obtained from the *fabric tensor* defined as

$$F_{ij} = \langle n_i n_j \rangle, \tag{7}$$

where $\vec{n}$ is the unit contact normal. By definition, we have $tr(\boldsymbol{F}) = 1$, and the largest eigenvalue F_1 occurs along the compression axis. The two other eigenvalues are $F_2 = F_3 = (1 - F_1)/2$. We define

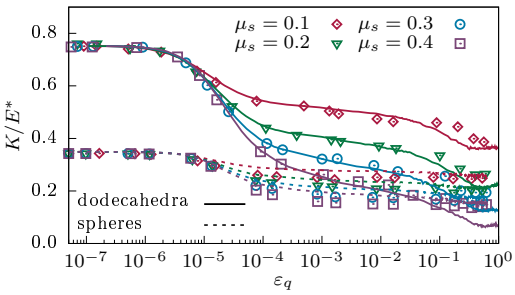

Fig. 6 Normalized bulk modulus as a function of shear strain ε_q for packings of spherical and dodecahedral particles with different values of friction coefficient μ_s. The lines are predictions by our proposed expression (29).

the contact anisotropy as [10, 47, 48]

$$a_c = 5(F_1 - F_2)/2. \tag{8}$$

The fabric tensor can be evaluated from the probability distribution $P(\vec{n})$ of the unit contact normal $\vec{n}$. In 3D, the contact normal $\vec{n}$ is parametrized by two angles $\theta \in [0; \pi]$ and $\phi \in [0; 2\pi]$. The probability density function $P(\Omega)$ of contact normals provides a detailed statistical information about the fabric, where $\Omega = (\theta, \phi)$ is the solid angle, with $d\Omega = \sin\theta d\theta d\phi$. The fabric tensor can then be expressed as [10, 45, 49, 50]:

$$F_{ij} = \int_\Omega n_i n_j P(\Omega) d\Omega = \frac{1}{N_c} \sum_{c \in V} n_i^c n_j^c, \tag{9}$$

where i and j design the components in a reference frame, and N_c is the total number of contacts in the control volume V. Under axi-symmetric conditions, the probability density function is independent of the azimuth angle ϕ. So, within a second-order harmonic approximation, we have

$$P(\Omega) = \frac{1}{4\pi} \left[1 + a_c(3\cos^2\theta - 1)\right]. \tag{10}$$

From Eqs. (9) and (10), and given the unit contact normal $\vec{n} = (\cos\theta, \sin\theta\cos\phi, \sin\theta\sin\phi)$, the eigenvalues of the fabric tensor are given by

$$F_1 = \int_\Omega n_1^2 P(\Omega) d\Omega = \frac{5 + 4a_c}{15}, \tag{11a}$$

$$F_2 = F_3 = \int_\Omega n_2^2 P(\Omega) d\Omega = \frac{5 - 2a_c}{15}. \tag{11b}$$

While the definitions of Z and a_c are straightforward in the case of spherical particles, we need

to consider the contact types for polyhedral particles, as discussed in Section 2. We generalize the coordination number by attributing different weights to different contact types. In particular, we define here a *constraint number* Z_c by weighing each contact type by the number of constraints it represents:

$$Z_c = 2(N_s + 2N_d + 3N_t)/N_p, \qquad (12)$$

where N_s, N_d, and N_t are the numbers of simple, double, and triple contacts, respectively, and N_p is the total number of particles. The constraint number is reduced to the coordination number in the case of spherical particles.

A packing of frictionless particles is isostatic so that the number of degrees of freedom per particle must be equal to the number of constraints per particle $Z_c/2$. The number of degrees of freedom is 3 per particle in the case of frictionless spheres (the rotations being ineffective), whereas polyhedra have 6 degrees of freedom per particle both with and without friction. Hence, the constraint number for packings of spheres and polyhedra is 6 and 12, respectively. We find $Z_c \simeq 6.03$ for spheres and $Z_c \simeq 12.05$ for polyhedra at the end of isotropic compaction, both remarkably close to the expected values. The small difference is due to the finite stiffness and overlaps between particles. This suggests that Z_c is the relevant connectivity parameter for polyhedral particle packings, in contrast to Z which has a lower value ($\simeq 8$) in the isostatic state. The same remarks apply to the definition of fabric tensor for polyhedra by considering that face-face contacts are equivalent to 3 contact points and edge-face contacts to 2 contact points.

Figure 7 displays the evolution of Z_c and a_c during compression. Consistently with the elastic moduli, at small shear strains ($< 10^{-5}$), both Z_c and $a_c \simeq 0$ (initially isotropic state) are constant and independent of μ_s due to the stability of the contact network. With the onset of particle rearrangements, Z_c decreases and tends to a constant value whereas a_c initially increases as a result of the loss of contacts perpendicular to the compression axis [6, 51]. The fabric anisotropy is larger in packings of polyhedral particles compared to spheres, and its peak value increases with μ_s.

The microstructure evolves also in terms of the distribution of different types of contacts. Fig. 8 displays a snapshot of force chains in the isotropic (initial) state and near the stress peak with different colors for different contact types. The proportions N_t/N_c of face-face contacts declines from 0.14 in the isotropic state to 0.1 in the peak state although we distinctly observe columnar force chains of face-face contacts along the compression axis in the peak state. In a similar vein, the proportion N_d/N_c of edge-face contacts declines during compression. Hence, the larger proportion of single contacts near the stress peak is the necessary condition for the stability of columnar force chains [52].

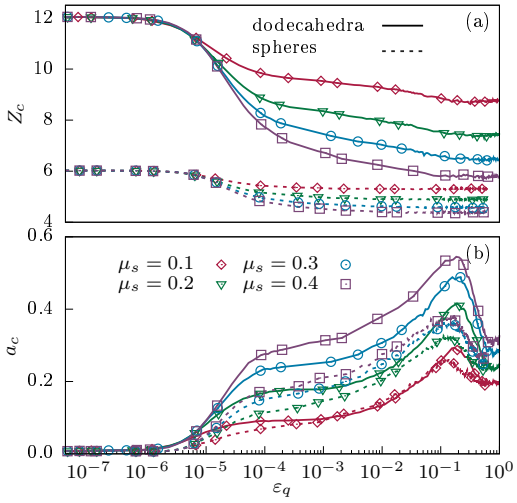

Fig. 7 Constraint number Z_c (a) and fabric anisotropy a_c (b) as a function of shear strain ε_q for packings of spherical and dodecahedral particles and different values of friction coefficient μ_s. The dashed and solid lines are for packings of spheres and dodecahedra, respectively. The symbols represent instances where strain probes were applied.

6 Relation between elastic moduli and microstructure

The central issue that we address here is whether the values of elastic moduli shown in Figs. 4, 5, and 6 can be univocally expressed in terms of Z_c and a_c. The connection between elasticity and granular microstructure has been previously investigated in the case of isotropic packings of spherical particles and compared with the predictions of EMT [19, 23, 26, 43]. We first derive analytical expressions of elastic moduli in the EMT framework for anisotropic media with orthotropic symmetry.

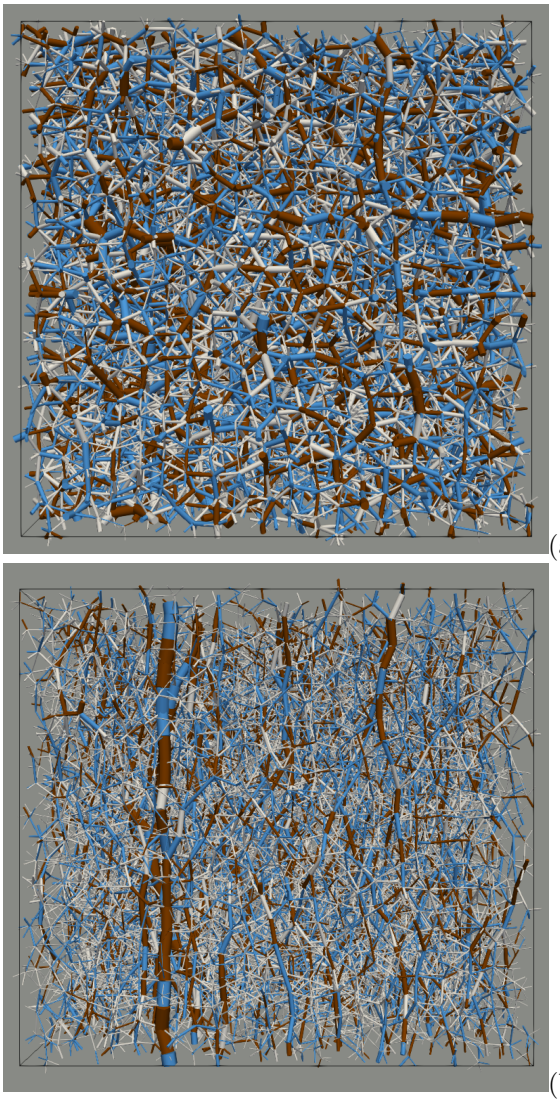

Fig. 8 Snapshot of the normal force network of a dodecahedral particle packing at isotropic state (a), and near stress peak (b) with friction coefficient $\mu_s = 0.1$. Line thickness is proportional to normal force. Single contacts are in white, double contacts in blue, and triple contacts in brown. The compression axis is along the vertical direction. At isotropic state, the fractions of single, double and triple contacts are 0.5, 0.36, and 0.14, respectively. At stress peak state, they are 0.59, 0.31, and 0.1, respectively.

Then, we compare our simulation data with its predictions to propose a general expression which correctly predicts the evolution of elastic moduli all along triaxial compression from the isostatic state up to the stress peak state.

6.1 Elastic moduli from EMT

The medium is assumed to behave as a continuum with particle centers moving according to the applied strain field (affine assumption). Hence, in response to an incremental strain $\delta\varepsilon_{ij}$, the normal and tangential displacements at each contact are simply given by

$$\delta_n = \delta\varepsilon_{ij} n_i n_j, \tag{13}$$
$$\delta_t = \delta\varepsilon_{ij} n_i t_j, \tag{14}$$

where $\vec{t}$ represents a tangential unit vector. The contact forces can therefore be obtained from these displacements and the force laws (1) and (2).

Let $(\vec{n'}, \vec{t'}, \vec{s'})$ be a local frame associated with the branch vector $\vec{\ell} = \ell\vec{n'}$ joining the centers of two touching particles. In spherical coordinates, we have

$$\begin{cases} \vec{n'} = (\cos\theta, \sin\theta\cos\phi, \sin\theta\sin\phi), \\ \vec{t'} = (-\sin\theta, \cos\theta\cos\phi, \cos\theta\sin\phi), \\ \vec{s'} = (0, -\sin\phi, \cos\phi), \end{cases} \tag{15}$$

where ϕ is the azimuth and θ is the latitude.

By affine assumption, the variation of ℓ is given by

$$\delta\vec{\ell} = \ell\boldsymbol{\varepsilon}\vec{n'}. \tag{16}$$

This variation leads to relative displacements δ_n, δ_t, and δ_s at any contact point between the two particles with its associated frame $(\vec{n}, \vec{t}, \vec{s})$, $\vec{n}$ being normal unit vector to the contact plane. For spherical particles, this frame exactly coincides with the frame associated with the branch vector. Due to disorder, this property holds also on average in the case of two convex particles. Indeed, we checked that in our samples, we have $\vec{n}\cdot\vec{n'} \simeq 1$. For this reason, we can use the contact frame together with the branch vector length to approximate the relative displacements at contact points:

$$\begin{cases} \delta_n = \ell\boldsymbol{\varepsilon}\vec{n}\cdot\vec{n}, \\ \delta_t = \ell\boldsymbol{\varepsilon}\vec{n}\cdot\vec{t}, \\ \delta_s = \ell\boldsymbol{\varepsilon}\vec{n}\cdot\vec{s}. \end{cases} \tag{17}$$

From the contact displacements, we write down the elastic energy per unit volume ΔW_e as a function of the strain tensor $\boldsymbol{\varepsilon}$. Let k_n and k_t be the normal stiffness and tangential stiffness,

respectively, and $n_c = N_c/V$ the contact number density in a volume V containing N_c contacts. Then, we have

$$\begin{aligned}\Delta W_e &= \frac{n_c k_n}{2}\langle\delta_n^2\rangle + \frac{n_c k_t}{2}\langle\delta_t^2\rangle + \frac{n_c k_t}{2}\langle\delta_s^2\rangle \\ &= \frac{n_c}{2}\langle\ell^2\rangle[k_n\langle(\boldsymbol{\varepsilon}\vec{n}\cdot\vec{n})^2\rangle + k_t\langle(\boldsymbol{\varepsilon}\vec{n}\cdot\vec{t})^2\rangle + k_t\langle(\boldsymbol{\varepsilon}\vec{n}\cdot\vec{s})^2\rangle]\end{aligned} \tag{18}$$

where it has been assumed that the branch vector length ℓ and contact orientation $\vec{n}$ are not correlated. Indeed, we checked that in our samples, we have $\langle\ell\cos^2\theta\rangle \simeq \langle\ell\rangle\langle\cos^2\theta\rangle$.

In the frame of the principal axes of the strain tensor $\boldsymbol{\varepsilon}$, we have

$$\begin{cases}\boldsymbol{\varepsilon}\vec{n}\cdot\vec{n} = \varepsilon_{11}\cos^2\theta + \varepsilon_{22}\sin^2\theta\cos^2\phi + \varepsilon_{33}\sin^2\theta\sin^2\phi, \\ \boldsymbol{\varepsilon}\vec{n}\cdot\vec{t} = \dfrac{1}{2}\sin 2\theta(-\varepsilon_{11} + \varepsilon_{22}\cos^2\phi + \varepsilon_{33}\sin^2\phi), \\ \boldsymbol{\varepsilon}\vec{n}\cdot\vec{s} = \dfrac{1}{2}\sin\theta\sin 2\phi(\varepsilon_{33} - \varepsilon_{22}).\end{cases} \tag{19}$$

The average values $\langle(\boldsymbol{\varepsilon}\vec{n}\cdot\vec{n})^2\rangle$, $\langle(\boldsymbol{\varepsilon}\vec{n}\cdot\vec{t})^2\rangle$, and $\langle(\boldsymbol{\varepsilon}\vec{n}\cdot\vec{s})^2\rangle$ are evaluated by integrating their expressions from Eq. (19) over the angles θ and ϕ by using the probability distribution function $P(\theta,\phi)$ given by Eq. (10). Once inserted in Eq. (18), an expression of the total elastic energy ΔW_e is obtained as a function of n_c, fabric anisotropy a_c, contact parameters, and strain tensor coefficients.

By definition, the elastic moduli C_{ij} are the second derivatives of this energy function with respect to ε_{ij}:

$$\begin{cases} C_{11} = \dfrac{\partial^2\Delta W_e}{\partial\varepsilon_{11}^2} = n_c\langle\ell^2\rangle k_n\left(\dfrac{3+2\alpha_t}{15} + \dfrac{24+4\alpha_t}{105}a_c\right), \\ C_{22} = \dfrac{\partial^2\Delta W_e}{\partial\varepsilon_{22}^2} = n_c\langle\ell^2\rangle k_n\left(\dfrac{3+2\alpha_t}{15} - \dfrac{12+2\alpha_t}{105}a_c\right), \\ C_{12} = \dfrac{\partial^2\Delta W_e}{\partial\varepsilon_{11}\partial\varepsilon_{22}} = n_c\langle\ell^2\rangle k_n\,(1-\alpha_t)\left(\dfrac{1}{15} + \dfrac{2}{105}a_c\right), \\ C_{23} = \dfrac{\partial^2\Delta W_e}{\partial\varepsilon_{22}\partial\varepsilon_{33}} = n_c\langle\ell^2\rangle k_n\,(1-\alpha_t)\left(\dfrac{1}{15} - \dfrac{4}{105}a_c\right), \end{cases} \tag{20}$$

where $\alpha_t = k_t/k_n$ is the stiffness ratio.

The shear moduli C_{55} and C_{44} are given by the second derivatives of the energy function with respect to the variables $\varepsilon_q = \varepsilon_{11} - \varepsilon_{22}$ and $\varepsilon_{q'} = \varepsilon_{22} - \varepsilon_{33}$:

$$\begin{cases} C_{55} = \dfrac{\partial^2\Delta W_e}{\partial\varepsilon_q^2} = \dfrac{n_c\langle\ell^2\rangle k_n}{30}\left(2 + 3\alpha_t + \dfrac{4+3\alpha_t}{7}a_c\right), \\ C_{44} = \dfrac{\partial^2\Delta W_e}{\partial\varepsilon_{q'}^2} = \dfrac{n_c\langle\ell^2\rangle k_n}{30}\left(2 + 3\alpha_t - \dfrac{8+6\alpha_t}{7}a_c\right). \end{cases} \tag{21}$$

Finally, the bulk modulus K is the second derivative of the energy function with respect to the volumetric strain $\varepsilon_v = \varepsilon_{11} + \varepsilon_{22} + \varepsilon_{33}$,

$$K = \frac{\partial^2\Delta W_e}{\partial\varepsilon_v^2} = \frac{n_c\langle\ell^2\rangle k_n}{9}. \tag{22}$$

Note that, we have $C_{22} - C_{23} = 2C_{44}$, so that the bulk modulus can be expressed as a function of C_{ij}:

$$K = \frac{C_{11} + 4C_{12} + 2C_{22} + 2C_{23}}{9}. \tag{23}$$

6.2 Comparison with numerical results

The above expressions of elastic moduli based on EMT are proportional to the number density n_c of contacts. It is easy to show that

$$n_c = \frac{Z_c\Phi}{2V_p}, \tag{24}$$

where V_p is the average particle volume. Furthermore, the elastic moduli can be normalized by E^*, which defines the reference value of all elastic moduli. Hence, following Eq. (22), the bulk modulus K^{EMT} can be expressed as

$$K^{EMT} = mE^*\Phi Z_c, \tag{25}$$

where

$$m = \frac{\langle\ell^2\rangle d}{18V_p}. \tag{26}$$

Equation (25) suggests that the bulk modulus is proportional to ΦZ_c with a prefactor depending mainly on the mean square distance $\langle\ell^2\rangle$ between particle centers. This expression of K is the same as the one derived previously for isotropic granular materials composed of spherical particles [19, 23]. Here, it is extended to polyhedral particles by replacing Z by Z_c. Figure 9 shows K as a function of ΦZ_c from all our simulation data at different instances of compression. The EMT prediction

is also plotted for comparison with the values of $\langle \ell^2 \rangle$ extracted from the simulations. All our data points, independently of friction coefficient, nicely collapse on a straight line for both spherical and polyhedral particle packings, as predicted by EMT, in exception to data points lying slightly above the line at low values of ΦZ_c. These data points represent actually the late stages of compression where the system is in the post-peak softening regime with intense particle rearrangements, leading to an over-estimation of elastic moduli.

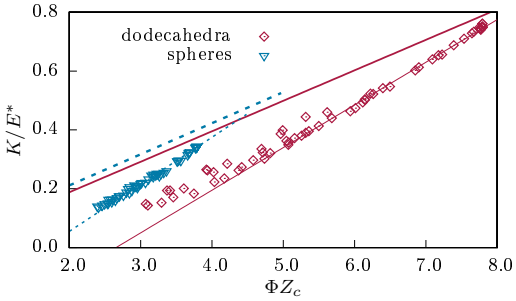

Fig. 9 Normalized bulk modulus K/E^* as a function of ΦZ_c from simulations of dodecahedral and spherical particle packings. The thin lines are linear fits to the data. The thick lines represent predictions of EMT for polyhedra (solid line) and spheres (dashed line).

While the predicted linear dependence of elastic moduli on ΦZ_c is in agreement with the simulation results, there are two key differences between the predicted values of bulk modulus K^{EMT} and the values measured in simulations for both spherical and polyhedral particle packings. First, the prefactor m is higher in the simulations. Secondly, K^{EMT} vanishes only when $Z_c\Phi$ tends to zero whereas in the simulations the bulk modulus vanishes for a finite value of $Z_c\Phi$. This means that the bulk modulus can be approximated as

$$K = E^*(n + m\Phi Z_c), \tag{27}$$

where n is a parameter of negative value which depends on particle shape. The fitted values of n and m are given in Table 1 for different particle shapes together with the values predicted by EMT. The differences between the EMT prediction and the simulated values of n and m have their origin in the nonaffine relative particle displacements which contradict the EMT assumption of an affine displacement field [19, 21]; see below.

Interestingly, the non-zero value of n in the linear fit to the simulation data implies that K vanishes at $\Phi Z_c = -n/m$. This ratio is $\simeq 2.6$ for polyhedra and $\simeq 1.65$ for spheres. The vanishing of K for a finite value of ΦZ_c is a reminiscent of unjamming transition at a finite value of Z_c. Obviously, unjamming does not occur in our system during compression but Fig. 9 shows that the lowest values of ΦZ_c ($\simeq 2.4$ for spheres and $\simeq 3.1$ for polyhedra) occur during post-peak softening and they are close to the values of $-n/m$.

According to Eqs. (20) and (21), all elastic moduli C_{ij} are proportional to K and their ratio depends linearly on the contact orientation anisotropy a_c:

$$C_{ij} = K(r_{ij} + s_{ij}a_c), \tag{28}$$

where the parameters r_{ij} and s_{ij} depend on particle shape. This linear dependence on fabric anisotropy is indeed what we observe in Fig. 10 for all elastic moduli and for both polyhedral and spherical particle packings, but with values of r_{ij} and s_{ij} that deviate from those predicted by EMT due to nonaffine displacement field; see Table 1.

6.3 General expression of elastic moduli

Based on the simulation data and effective medium theory discussed previously, we propose the following analytical expression for the five orthotropic elastic moduli:

$$C_{ij} = E^*(n + m\Phi Z_c)(r_{ij} + s_{ij}a_c). \tag{29}$$

The EMT predictions of n, m, r_{ij}, and s_{ij} are shown in Table 1 together with their values measured from our simulations for the three particle shapes. This expression relates in a univocal way the elastic moduli to the microstructure of granular materials under transversely isotropic symmetry. With its parameter values given in Table 1, it allows us to predict the evolution of elastic moduli as a function of shear strain ε_q from that of Z_c and a_c extracted from simulations. Figures 4, 5, and 6 show the evolution of the elastic moduli according to this analytical expression together

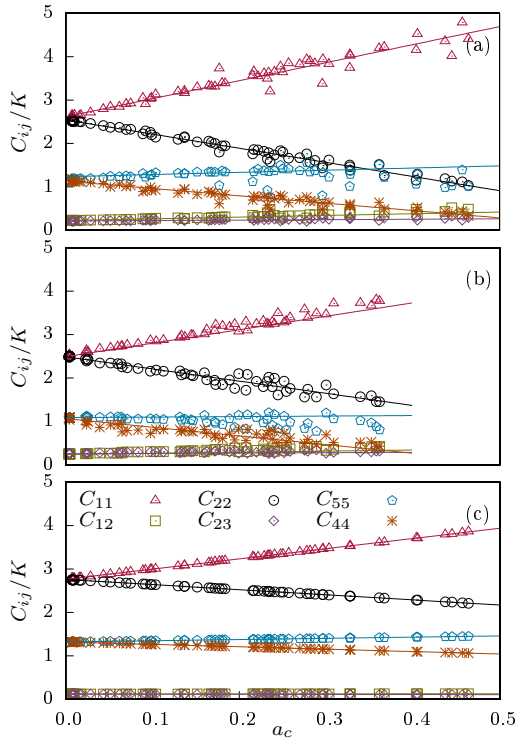

Fig. 10 Normalized moduli C_{ij}/K as a function of fabric anisotropy a_c for the dodecahedral (a) and spherical (b) particle packings from simulations with different values of the friction coefficient, together with theoretical prediction (c) based on the EMT. The straight lines are the best linear fits to the data points. The data of icosahedra is shown in Supplemental Material and it follows a similar evolution.

with their measured values from simulations. We see that this expression follows amazingly well the simulation data from the isostatic state up to the stress peak state. The observed "wavy" feature of the evolution of elastic moduli observed in these figures can therefore be explained as a consequence of the multiplicative contributions of the isotropic part $n + m\Phi Z_c$ and the anisotropic part $r_{ij} + s_{ij}a_c$ with decreasing Z_c and increasing a_c during compression.

It is remarkable that the model parameters n, m, r_{ij}, and s_{ij} are independent of friction coefficient. The differences between elastic moduli for different values of μ_s arise therefore from the effect of the latter on the evolution of Z_c and a_c. The values of parameters in Table 1 show also that the higher value of K in the case of polyhedral particle packings compared to that of the sphere packing is mainly due to the higher values of $Z_c\Phi$ rather than the smaller variations of the model parameters. Furthermore, the dodecahedral and icosahedral particle packings have slightly different elastic moduli. A detailed comparison between the elastic moduli of polyhedral particle packings with different numbers of faces will be presented elsewhere.

The observed linear dependence of the elastic moduli on $Z_c\Phi$ and a_c in our simulations suggests that, despite the evolution of the microstructure the level of nonaffine displacements is nearly constant during triaxial compression. To check this point, we investigated the nonaffine displacements in our simulations. Several methods can be used to quantify the level of nonaffinity [53–56]. We used a measure of non-affinity from the relative particle displacements. Let $\delta r_z^\alpha = \delta r_z^i - \delta r_z^j$ be the relative displacement at the contact α between particles i and j projected along the z direction and ℓ^α the length of the branch vector joining their centers. Then, the actual strain increment at contact α along the z direction is $\delta\varepsilon_z^\alpha = \delta r_z^\alpha/\ell^\alpha$. We define the nonaffinity ξ along the compression axis as

$$\xi = \frac{\sqrt{\langle(\delta\varepsilon_z)^2\rangle - \langle\delta\varepsilon_z\rangle^2}}{\langle\delta\varepsilon_z\rangle}, \qquad (30)$$

where the averages run over all contacts inside the packing. Note also that the average $\langle\delta\varepsilon_z\rangle$ is simply equal to the mean affine displacement imposed when probing the elastic response.

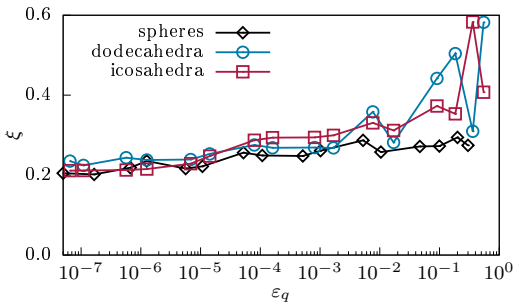

Fig. 11 Level of non-affinity ξ (equation (30)) as a function of shear strain ε_q for packings of spherical and dodecahedral particles with friction coefficient $\mu_s = 0.1$.

We calculated ξ at all probing instances and Fig. 11 displays its evolution for the three particle shapes in the case $\mu_s = 0.1$ (the evolution being similar for other values of μ_s). Interestingly, ξ has nearly the same value for all shapes during compression and increases slowly from $\simeq 0.2$ at low

compression until the stress peak at $\varepsilon_q \simeq 5\times10^{-2}$. Beyond this point, it grows rapidly to higher values as a result of softening and unstable particle motions. This is consistent with the evolution of the elastic moduli shown in Fig. 9, where the corresponding data points deviate from expression (29). The nearly constant level of non-affinity before stress peak explains the linear dependence of elastic moduli on the microstructural prameters Z_c and a_c and thus the constant values of the parameters n, m, r_{ij}, and s_{ij} in the analytical expression (29) implying that their values are almost only functions of particle shape. Obviously, the small second-order effects arising from the dependence of non-affinity on the increasing anisotropy of the packing during compression are not observable within the statistical precision of our simulation data.

7 Conclusion

We derived a general expression (29) of the orthotropic elastic moduli of granular materials under triaxial boundary conditions as a function of microstructural parameters for three different particle shapes and four different values of the interparticle friction coefficient. This expression reveals three different origins of elastic moduli: a stress scale E^*, an isotropic part, and an anisotropic part. The stress scale E^* depends on the force model. In our linear force model, its value is simply k_n/d, but for a Hertz contact, which is obviously not adapted to faceted particles, it should be multiplied by a ratio $\{p/(\tilde{E}Z_c\Phi)\}^{1/3}$, where $\tilde{E} = E/(1-\nu^2)$ is the reduced elastic modulus [20, 23, 24], and makes depend the moduli on the confining pressure.

The effect of particle shape appears at two levels: on the one hand, through the parameters n, m, r_{ij}, and s_{ij}, which do not depend on friction coefficient and are not neither expected to depend on p for Hertzian contacts, and on the other hand, through the microstructure via the values of Z_c and a_c, which depend on both particle shape and friction coefficient μ_s. While the expression (29) provides a powerful model of elastic moduli in the hardening regime (before stress peak) with a clear distinction between the two effects of particle shape, our results indicate that, due to unstable particle rearrangements, the measurement of elastic moduli in the softening regime requires strain probes well below 10^{-5} used in this work throughout triaxial compression.

The expression (29) makes it possible to extract the values of Z_c and a_c and the model parameters n, m, r_{ij}, and s_{ij} from experimental measurements of the elastic moduli. This is specially relevant for granular materials composed of aspherical particle shapes whose elastic properties have not yet been a subject of systematic investigation. More work is currently underway to further validate Eq. (29) for other particle shapes, different values of the stiffness ratio, and different boundary conditions. A detailed comparison of the elastic moduli of polyhedral particle packings with increasing number of faces will be published in a forthcoming paper.

Acknowledgments. We warmly thank Carlos Santamarina for fruitful discussions. The authors acknowledge financial support by SIFCO project (CEA), EDF, and ORANO.

References

[1] Jaeger, H. M., Nagel, S. R. & Behringer, R. P. The physics of granular materials. *Physics Today* **49**, 32–38 (1996). URL https://doi.org/10.1063/1.881494.

[2] Herrmann, H. J., Hovi, J.-P. & Luding, S. *Physics of dry granular media* Vol. 350 (Springer Science & Business Media, 2013).

[3] Radjai, F., Roux, J.-N. & Daouadji, A. Modeling granular materials: Century-long research across scales. *J. Eng. Mech.* **143**, 04017002 (2017).

[4] Donev, A. *et al.* Improving the density of jammed disordered packings using ellipsoids. *Science* **303**, 990–993 (2004). URL https://doi.org/10.1126/science.1093010.

[5] Cleary, P. The effect of particle shape on simple shear flows. *Powder Technology - POWDER TECHNOL* **179**, 144–163 (2008).

[6] Azéma, E., Radjai, F. & Saussine, G. Quasistatic rheology, force transmission and fabric properties of a packing of irregular polyhedral particles. *Mechanics of Materials* **41**, 729–741 (2009).

[7] Azéma, E. & Radjaï, F. Stress-strain behavior and geometrical properties of packings of elongated particles. *Physical Review E* **81**, 051304 (2010).

[8] Saint-Cyr, B., Delenne, J.-Y., Voivret, C., Radjai, F. & Sornay, P. Rheology of granular materials composed of nonconvex particles. *Phys. Rev. E* **84**, 041302 (2011). URL https://link.aps.org/doi/10.1103/PhysRevE.84.041302.

[9] CEGEO *et al.* Particle shape dependence in 2d granular media. *Europhysics Letters* **98**, 44008 (2012). URL https://dx.doi.org/10.1209/0295-5075/98/44008.

[10] Azéma, E., Radjai, F. & Dubois, F. Packings of irregular polyhedral particles: strength, structure, and effects of angularity. *Physical Review E* **87**, 062203 (2013).

[11] Athanassiadis, A. G. *et al.* Particle shape effects on the stress response of granular packings. *Soft Matter* **10**, 48–59 (2014). URL http://dx.doi.org/10.1039/C3SM52047A.

[12] Wegner, S. *et al.* Effects of grain shape on packing and dilatancy of sheared granular materials. *Soft Matter* **10**, 5157–5167 (2014). URL http://dx.doi.org/10.1039/C4SM00838C.

[13] Nguyen, D.-H., Azéma, É., Radjai, F. & Sornay, P. Effect of size polydispersity versus particle shape in dense granular media. *Physical Review E* **90**, 012202 (2014).

[14] Nguyen, D.-H., Azéma, E., Sornay, P. & Radjai, F. Effects of shape and size polydispersity on strength properties of granular materials. *Physical Review E* **91**, 032203 (2015).

[15] Zhao, S. & Zhou, X. Effects of particle asphericity on the macro- and micromechanical behaviors of granular assemblies. *Granular Matter* **19**, 38 (2017). URL https://doi.org/10.1007/s10035-017-0725-6.

[16] Kawamoto, R., Andò, E., Viggiani, G. & Andrade, J. All you need is shape: Predicting shear banding in sand with ls-dem. *Journal of the Mechanics and Physics of Solids* **111** (2017).

[17] Zhao, S. & Zhao, J. A poly-superellipsoid-based approach on particle morphology for dem modeling of granular media. *International Journal for Numerical and Analytical Methods in Geomechanics* **43**, 2147–2169 (2019).

[18] Marteau, E. & Andrade, J. E. An experimental study of the effect of particle shape on force transmission and mobilized strength of granular materials. *J. Appl. Mech* **88** (2021). URL https://doi.org/10.1115/1.4051818.

[19] Agnolin, I. & Kruyt, N. P. On the elastic moduli of two-dimensional assemblies of disks: Relevance and modeling of fluctuations in particle displacements and rotations. *Computers & Mathematics with Applications* **55**, 245–256 (2008).

[20] Agnolin, I. & Roux, J.-N. Internal states of model isotropic granular packings. iii. elastic properties. *Physical Review E* **76**, 061304 (2007).

[21] Kruyt, N. P., Agnolin, I., Luding, S. & Rothenburg, L. Micromechanical study of elastic moduli of loose granular materials. *Journal of the Mechanics and Physics of Solids* **58**, 1286–1301 (2010).

[22] La Ragione, L. & Magnanimo, V. Evolution of the effective moduli of an anisotropic, dense, granular material. *Granular Matter* **14**, 749–757 (2012).

[23] Khalili, M. H., Roux, J.-N., Pereira, J.-M., Brisard, S. & Bornert, M. Numerical study of one-dimensional compression of granular materials. ii. elastic moduli, stresses, and microstructure. *Physical Review E* **95**, 032908 (2017).

[24] Makse, H. A., Gland, N., Johnson, D. L. & Schwartz, L. Granular packings: Nonlinear elasticity, sound propagation, and collective relaxation dynamics. *Physical Review E* **70**, 061302 (2004).

[25] Agnolin, I., Jenkins, J. T. & La Ragione, L. A continuum theory for a random array of identical, elastic, frictional disks. *Mechanics of Materials* **38**, 687–701 (2006).

[26] Makse, H. A., Gland, N., Johnson, D. L. & Schwartz, L. M. Why effective medium theory fails in granular materials. *Physical Review Letters* **83**, 5070 (1999).

[27] Zaccone, A. & Scossa-Romano, E. Approximate analytical description of the nonaffine response of amorphous solids. *Physical Review B* **83**, 184205 (2011).

[28] Richefeu, V. & Villard, P. *Modeling gravity hazards from rockfalls to landslides* (Elsevier, 2016).

[29] Herrmann, H. & Luding, S. Modeling granular media on the computer. *Continuum Mechanics and Thermodynamics* **10**, 189–231 (1998).

[30] Thornton, C. & Antony, S. Quasi-static shear deformation of a soft particle system. *Powder technology* **109**, 179–191 (2000).

[31] Moreau, J. J. Sorne numerical methods in multibody dynamics: application to granular materials. *European Journal of Mechanics-A/Solids* **13**, 93–114 (1994).

[32] Radjai, F. & Richefeu, V. Contact dynamics as a nonsmooth discrete element method. *Mechanics of Materials* **41**, 715–728 (2009).

[33] Radjai, F. & Dubois, F. *Discrete-element modeling of granular materials* (Wiley-Iste, 2011).

[34] Richefeu, V., El Youssoufi, M. S. & Radjai, F. Shear strength properties of wet granular materials. *Physical Review E* **73**, 051304 (2006).

[35] Dippel, S., Batrouni, G. & Wolf, D. How transversal fluctuations affect the friction of a particle on a rough incline. *Physical Review E* **56**, 3645 (1997).

[36] Peyneau, P.-E. & Roux, J.-N. Solidlike behavior and anisotropy in rigid frictionless bead assemblies. *Physical Review E* **78**, 041307 (2008).

[37] Radjai, F. Multi-periodic boundary conditions and the contact dynamics method. *Comptes Rendus Mécanique* **346**, 263–277 (2018).

[38] Allen, M. P. & Tildesley, D. J. *Computer simulation of liquids* (Oxford university press, 2017).

[39] MIDI, G. On dense granular flows. *Eur. Phys. J. E* **14**, 341–365 (2004).

[40] Forterre, Y. & Pouliquen, O. Flows of dense granular media. *Annual Review of Fluid Mechanics* **40**, 1–24 (2008).

[41] Fast, L., Wills, J., Johansson, B. & Eriksson, O. Elastic constants of hexagonal transition metals: Theory. *Physical Review B* **51**, 17431 (1995).

[42] Lubarda, V. & Chen, M. On the elastic moduli and compliances of transversely isotropic and orthotropic materials. *Journal of Mechanics of Materials and Structures* **3**, 153–171 (2008).

[43] Kruyt, N. P. & Rothenburg, L. Micromechanical bounds for the effective elastic moduli of granular materials. *International Journal of Solids and Structures* **39**, 311–324 (2002).

[44] Ezaoui, A. & Benedetto, H. D. Experimental measurements of the global anisotropic elastic behaviour of dry hostun sand during triaxial tests, and effect of sample preparation. *Géotechnique* **59**, 621–635 (2009).

[45] Bathurst, R. J. & Rothenburg, L. Observations on stress-force-fabric relationships in idealized granular materials. *Mechanics of materials* **9**, 65–80 (1990).

[46] Radjai, F., Delenne, J.-Y., Azéma, E. & Roux, S. Fabric evolution and accessible geometrical states in granular materials. *Granular Matter* **14**, 259–264 (2012).

[47] Zhao, C.-F. & Kruyt, N. P. An evolution law for fabric anisotropy and its application in micromechanical modelling of granular materials. *International journal of solids and structures* **196**, 53–66 (2020).

[48] Radjai, F., Wolf, D. E., Jean, M. & Moreau, J.-J. Bimodal character of stress transmission in granular packings. *Physical review letters* **80**, 61 (1998).

[49] Oda, M. Initial fabrics and their relations to mechanical properties of granular material. *Soils and foundations* **12**, 17–36 (1972).

[50] Satake, M. Constitution of mechanics of granular materials through graph representation. *Theoretical and applied mechanics* **26**, 257–266 (1978).

[51] Rothenburg, L. & Kruyt, N. P. Critical state and evolution of coordination number in simulated granular materials. *International Journal of Solids and Structures* **41**, 5763–5774 (2004).

[52] Radjai, F., Wolf, D. E., Jean, M. & Moreau, J.-J. Bimodal character of stress transmission in granular packings. *Phys. Rev. Lett.* **80**, 61–64 (1998). URL https://link.aps.org/doi/10.1103/PhysRevLett.80.61.

[53] Broedersz, C. P., Mao, X., Lubensky, T. C. & MacKintosh, F. C. Criticality and isostaticity in fibre networks. *Nature Physics* **7**, 983–988 (2011).

[54] Broedersz, C., Sheinman, M. & MacKintosh, F. Filament-length-controlled elasticity in 3d fiber networks. *Physical review letters* **108**, 078102 (2012).

[55] Head, D. A., Levine, A. J. & MacKintosh, F. Deformation of cross-linked semiflexible polymer networks. *Physical review letters* **91**, 108102 (2003).

[56] Mathesan, S., Tripathy, M., Srivastava, A. & Ghosh, P. Non-affine deformation of free volume during strain dependent diffusion in polymer thin films. *Polymer* **155**, 177–186 (2018).

	C_{11}		C_{22}		C_{12}		C_{23}		C_{44}		C_{55}		K	
	r_{11}	s_{11}	r_{22}	s_{22}	r_{12}	s_{12}	r_{23}	s_{23}	r_{44}	s_{44}	r_{55}	s_{55}	n	m
EMT (expression)	$\frac{9+6\alpha_t}{5}$	$\frac{72+12\alpha_t}{35}$	$\frac{9+6\alpha_t}{5}$	$-\frac{36+6\alpha_t}{35}$	$\frac{3-3\alpha_t}{5}$	$\frac{6-6\alpha_t}{35}$	$\frac{3-3\alpha_t}{5}$	$-\frac{12-12\alpha_t}{35}$	$\frac{6+9\alpha_t}{10}$	$-\frac{12+9\alpha_t}{35}$	$\frac{6+9\alpha_t}{10}$	$\frac{12+9\alpha_t}{70}$	0	$\frac{\langle\ell^2\rangle d}{18V_p}$
EMT (value)	2.760	2.332	2.760	-1.166	0.120	0.034	0.120	-0.069	1.320	-0.549	1.320	0.274	0	0.105
Simulation (dodecahedra)	2.617	4.151	2.542	-3.258	0.225	0.387	0.213	0.100	1.132	-1.694	1.234	0.500	-0.378	0.145
Simulation (icosahedra)	2.547	4.565	2.563	-3.482	0.223	0.500	0.215	0.200	1.154	-2.176	1.172	0.932	-0.400	0.150
Simulation (spheres)	2.490	3.105	2.490	-2.812	0.240	0.255	0.250	0.080	1.065	-2.000	1.087	0.120	-0.265	0.160

Table 1 Fitting parameters in Eq. (29) for elastic moduli from the effective medium theory (EMT) and DEM simulations of the three particle shapes.